Computational Neuroscience

Source modeling of ElectroCorticoGraphy (ECoG) data: Stability analysis and spatial filtering

A. Pascarella [a,*], C. Todaro [b], M. Clerc [c], T. Serre [d], M. Piana [e,f]

[a] CNR – IAC, Roma, Italy
[b] Department of Neuroscience, Imaging and Clinical Sciences, Institute for Advanced Biomedical Technologies, University "G. d'Annunzio" of Chieti-Pescara, Italy
[c] INRIA Sophia Antipolis – Mediterranee, France
[d] Brown University, USA
[e] Department of Mathematics, University of Genova, Italy
[f] CNR – SPIN, Genova, Italy

H I G H L I G H T S

- First application of a spatial filter to ECoG data.
- The ECoG inverse problem turns out to be numerically stable.
- Beamformers give reliable estimates of neural current even for dipoles far from the grid.
- The reconstructed brain activity seems consistent with monkey and human studies.

A R T I C L E I N F O

A B S T R A C T

Background: Electrocorticography (ECoG) measures the distribution of the electrical potentials on the cortex produced by the neural currents. A full interpretation of ECoG data requires solving the ill-posed inverse problem of reconstructing the spatio-temporal distribution of the neural currents. This study addresses the ECoG source modeling developing a beamformer method.
New method: We computed the lead-field matrix by using a novel routine provided by the OpenMEEG software. We performed an analysis of the numerical stability of the ECoG inverse problem by computing the condition number of the lead-field matrix for different configurations of the electrodes grid. We applied a Linear Constraint Minimum Variance (LCMV) beamformer to both synthetic data and a set of real measurements recorded during a rapid visual categorization task.
Results: For all considered grids the condition number indicates that the ECoG inverse problem is mildly ill-conditioned. For realistic SNR we found a good performance of the LCMV algorithm for both localization and waveforms reconstruction.
Comparison with existing method: The flow of information reconstructed by analyzing real data seems consistent with both invasive monkey electrophysiology studies and non-invasive (MEG and fMRI) human studies.
Conclusions: Despite a growing interest from the neuroscientific community, solving the ECoG inverse problem has not quite yet reached the level of systematicity found for EEG and MEG. Starting from an analysis of the numerical stability of the problem we considered the most widely utilized method for modeling neurophysiological data based on the beamformer method in the hope to establish benchmarks for future studies.

© 2016 Elsevier B.V. All rights reserved.

1. Introduction

ElectroCorticoGraphy (ECoG) consists in recording neural activity using electrodes placed directly on the exposed surface of the brain – from just above (epidural) or just under (subdural) the dura mater. ECoG arrays consist of sterile, disposable, stainless steel

* Corresponding author at: IAC-CNR, Via dei Taurini 19, 00185 Roma, Italy.
Tel.: +39 06 49270946; fax: +39 06 4404306.
E-mail address: a.pascarella@iac.cnr.it (A. Pascarella).

electrodes (Schalk and Leuthardt, 2011; Schuh and Drury, 1997). The neuroscientific and clinical effectiveness of ECoG investigation should be compared to that of related non-invasive techniques such as electroencephalography (EEG) (Michel et al., 2004), which consists in recording electrical potentials directly on the scalp, and magnetoencephalography (MEG) (Hämäläinen et al., 1993), which consists of recording the magnetic fields produced by the neural activity outside the head. In both cases, ECoG achieves both better spatial resolution (below 1 cm) and better signal-to-noise ratio (Schalk and Leuthardt, 2011). For this reason, ECoG has frequently been used to validate findings from the EEG and MEG literature (Huiskamp, 2002).

As for EEG and MEG, a full interpretation of ECoG data requires solving an inverse problem in order to reconstruct the neural currents inside the whole brain, in both space and time, from ECoG signals recorded from a limited number of positions close to the cortical surface. Despite a growing interest from the neuroscientific community, existing methods for ECoG source modeling are not yet as systematic and optimized as for EEG and MEG. For example, Fuchs et al. (2007) applied the minimum norm estimation (MNE) method (Hämäläinen and Ilmoniemi, 1984) to both simulated datasets and interictal recordings of epileptic patients, demonstrating that source imaging methods can localize brain electrical sources with fairly high localization accuracy. They used a source model consisting of cortical patches and showed that a single-layer boundary element method (BEM) provides more accurate source estimates compared to a simpler spherical model. However, their model remained relatively simplistic because it describes the brain as a single layer. Zhang et al. (2008) applied a source reconstruction method based on MNE but considered a source space which included deep brain structures. These authors used a finite element method (FEM) to compute the forward model incorporating the scalp, the skull, the cerebral spinal fluid (CSF), the implanted elastic ECoG grids as well as the brain itself. The effectiveness of this approach was further demonstrated against MUltiple SIgnal Classification (MUSIC) (Mosher et al., 1992; Mosher and Leahy, 1998; Mosher and Leahy, 1999) by Dümpelmann et al. (2009). Cho et al. (2011) applied four different cortical source imaging algorithms based on the Tikhonov regularization framework. More specifically, they used MNE, low-resolution electromagnetic tomography (LORETA), standardized LORETA (sLORETA), and Lp-norm estimation (with $p = 1.5$) to analyze artificial ECoG datasets generated assuming various sizes for the source patches and various locations. They also applied these four algorithms to clinical recordings acquired from a pediatric epilepsy patient. Finally, Dümpelmann et al. (2012) addressed the question of which factors are relevant for reliable source reconstruction based on sLORETA.

In the present paper we studied the ECoG inverse problem starting from an analysis of its numerical stability. To this aim, we first updated the OpenMEEG software (available at http://openmeeg.github.io; Kybic et al., 2005; Gramfort et al., 2010) with a new function for the construction of the ECoG lead-field matrix. The lead-field matrix characterizes the linear transformation which maps the neural current intensity on the cortical mantle onto the electric potentials recorded by the ECoG sensors. Our routine utilizes BEM and interpolation methods to numerically solve the ECoG forward problem in the case of a three-layer head model that includes the scalp, the skull, and the brain. We then computed the condition number of the lead-field matrix, which provides a good quantitative measure of the numerical stability of the ECoG inverse problem, for different configurations of the electrodes' grid, characterized by different position, shape, and number of electrodes.

We finally addressed the ECoG source-modeling problem using a Linearly Constrained Minimum Variance (LCMV) beamformer

method (Van Veen et al., 1997) by identifying brain regions that contribute to the generation of the recorded signal while spatially filtering out those that do not. Beamformers currently represent the most widely utilized algorithm for modeling neurophysiological data (Spencer et al., 1992; Van Veen et al., 1997; Sekihara et al., 2001; Sekihara et al., 2002; Hillebrand and Barnes, 2005; Brookes et al., 2007; Quraan, 2011) and therefore constitute a good benchmark. We validated the accuracy and robustness of the LCMV beaformer against synthetic data simulated using the OpenMEEG framework as well as real ECoG measurements recorded during a rapid visual categorization task (Thorpe et al., 1996).

2. Methods

2.1. The ECoG forward problem

The ECoG forward problem can be formulated using Maxwell's equations under quasi-static approximation, which yields the classical electrostatic equation:

$$\nabla(\sigma \nabla V) = \nabla \cdot J^p \tag{1}$$

where J^p is the primary neural current, σ is the conductivity and V the electric potential inside a head Ω. Here, the ECoG electrodes are modeled as point-wise elements. The primary neural current field, which is assumed to reflect the postsynaptic activity of cortical pyramidal neurons, is modeled as a linear superposition of current dipoles, constrained to be normal to the cortical surface. The forward problem consists in finding the electric potential V generated at the EcoG electrode positions, for a given current density field J^p and given a complete knowledge of σ.

OpenMEEG is a C++ open source software package for solving the electromagnetic forward problem with a boundary element method (BEM), assuming a head domain Ω with piecewise constant conductivity while the electric potential V is represented on the boundaries of the regions of constant conductivity. This toolbox was originally developed to compute the lead-field matrix for solving the MEG and EEG forward problems, i.e. to determine the magnetic field outside the head and the electric potential on the scalp, respectively. In the ECoG case, the lead-field matrix linearly maps the current density J^p in the source space to the electrical potentials V in the sensor space, which is made of the nodes in the mesh. In order to compute this matrix, we have to define a head model consisting of the tissue conductivities, and a geometrical description (i.e. triangulated meshes) of the interfaces between these tissues. Here, we adopted a three-layer model, which includes the scalp, the skull and the brain, while neglecting inhomogeneities of the skull due to the foramina and craniotomy. Given the head model, OpenMEEG is used to compute the ECoG lead field matrix L by:

(i) Solving a symmetric linear system $AZ = H$ that represents a discretization of Eq. (1), where A has dimension $Q \times Q$ (Q is the number of points and triangles in the model), H has dimension $Q \times N$ (N is the number of discretization points on the cortex) and Z has dimension $Q \times N$ and contains the unknown potentials and normal currents discretized on each boundary; and

(ii) Applying an interpolation operator Ξ (with dimension $M \times Q$, where M is the number of sensors) to Z (computed in step (i) to infer the potentials at each electrode location.

The matrix $L = \Xi Z$ has dimension $M \times N$ and represents the ECoG lead-field matrix computed by the routine.

2.2. Conditioning of the lead-field matrix

Given the forward model described above, the lead field matrix L maps the source amplitude time series $s(t)$ at N locations in the brain to the measured potential time series $V(t)$:

$$V(t) = L \ s(t)$$
$$s(t) = [s_1(t), \ldots, s_N(t)]^T. \tag{2}$$

The inverse problem aims to reconstruct the N source amplitudes from M experimental observations, where N is typically far larger than M. Therefore it is quite natural to consider the least-squares problem associated to (2), whose minimum norm solution is the so-called generalized solution $s^+(t)$. The numerical stability of the ECoG inverse problem (2) is measured by the condition number of the lead-field matrix, i.e. the positive number $C(L)$ such that

$$\frac{\|\delta s^+(t)\|}{\|s^+(t)\|} \leq C(L) \frac{\|\delta V(t)\|}{\|V(t)\|} \tag{3}$$

It is easy to prove that:

$$C(L) = \frac{\sigma_1}{\sigma_q} \tag{4}$$

where σ_1 and σ_q are the biggest and smallest singular value of the lead-field matrix, respectively (see Golub and Van Loan (1996) for a proof).

2.3. The ECoG inverse problem

Owing to the fact that the condition number is typically large, the generalized solution is typically not a numerically stable estimate of the neural activity. As a result, the ECoG inverse problem must be addressed by means of some regularization method to find an optimal trade-off between stability and data fitting. Beamformers are the most frequently used regularization algorithms for the analysis of neurophysiological data. They are based on the idea that a good solution can be found by focusing the processing of individual source locations to explain the measured data while blocking signals from all other locations. This result is obtained by applying an appropriate weight vector to the signal time series, i.e. by computing

$$\hat{s}_n(t) = w^T(r_n)V(t) \tag{5}$$

where r_n denotes the position of the source, t is the time point and all the computational effort is to determine the weight vector (or filter) $w(r_n)$ in such a way that $\hat{s}_n(t)$ contains just the actual neural signal. In the case of the Linearly Constrained Minimum Variance (LCMV) beamformer (Van Veen et al., 1997), this weight vector is computing by minimizing the objective function:

$$w(r_n) = \arg\min_w w^T R w \tag{6}$$

over the set of weights which satisfy the constraint:

$$w^T l(r_n) = 1 \tag{7}$$

In Eq. (6), R is the covariance matrix estimated by

$$R = \frac{1}{T-1} V V^T \tag{8}$$

and $l(r_n)$ in Eq. (7) is the n-th column vector of the lead-field matrix L. The solution of the constrained optimization problem (6)–(8) is given by:

$$w(r_n) = [l(r_n)^T R^{-1} l(r_n)]^{-1} R^{-1} l(r_n) \tag{9}$$

It follows that a possible implementation of this LCMV beamformer is given by the following scheme:

1. For each grid point on the cortex, compute the neural activity index:

$$f(r_n) = \frac{[l(r_n)^T R^{-1} l(r_n)]^{-1}}{[l(r_n)^T l(r_n)]^{-1}} \tag{10}$$

2. Identify the points where the neural activity index reaches its local maximum.
3. For these points, compute the source waveforms using (5) and (9).

Furthermore, the LCMV beamformer can also be used to produce a complete map of neural activity over time by first computing the weight vector from Eq. (9) for all time points and locations.

3. Results

3.1. Numerical stability of the inverse problem

In order to quantify the numerical stability of the ECoG inverse problem, we studied the condition number of the lead-field matrix L for different grid positions. We constructed the lead-field matrices for four simulated grid placements on the frontal, parietal, occipital and fronto-parietal lobes, respectively (see Fig. 1). We used a head model provided by OpenMEEG, with a number of vertices on the brain cortex (16619) that provides a reasonable trade-off between the realism of the geometric foldings of the gray-white matter and the numerical complexity.

Each matrix has dimension M x N, where the number of electrodes M changes slightly depending on the grid placement adopted ($M = 55$ for the frontal grid, $M = 51$ for the parietal grid, $M = 53$ for the occipital grid and $M = 51$ for the frontal-parietal grid); the number of nodes N used to discretize the cortical source space (source nodes) is fixed to $N = 16,619$. We ran the source localization algorithm on each of the four electrode configurations. Fig. 2 contains histograms of the number of source nodes as a function of their mean distance from the grid (this distance was computed as the average of the distances between each source node and all the electrodes in the grid). This figure shows that the histograms corresponding to the occipital and fronto-parietal grids reach their peaks in correspondence of mean node-grid distances larger than the ones in the case of the frontal and parietal grids.

Table 1 compares the condition number of the lead-field matrix associated to the four grids with the one associated to a simulated experiment mimicking a whole-head EEG helmet with 60 channels. Also in this case the lead-field matrix has been computed within the OpenMEEG package, using the same number of source nodes as in the four simulated ECoG experiments and computing the electric potential on the scalp at 60 points according to a whole-head configuration.

The conditioning for the four ECoG grids remains relatively small ($<10^2$) and was found to be dependent on the grid placement with the highest value for the occipital grid and the smallest for the parietal grid. Also, the comparison with the EEG case shows that the intrinsic numerical instability of EEG is around one order of magnitude higher than that of ECoG, due to the signal attenuation caused by the low-conductive skull.

3.2. Numerical validation of the LCMV beamformer

We tested the performance of the LCMV beamformer against synthetic data for different noise levels. We considered two different experimental setups. We first placed a synthetic dipole located at one of the nodes of the cortical source space and assigned to it a Gaussian waveform with peak value 0.02 nAm
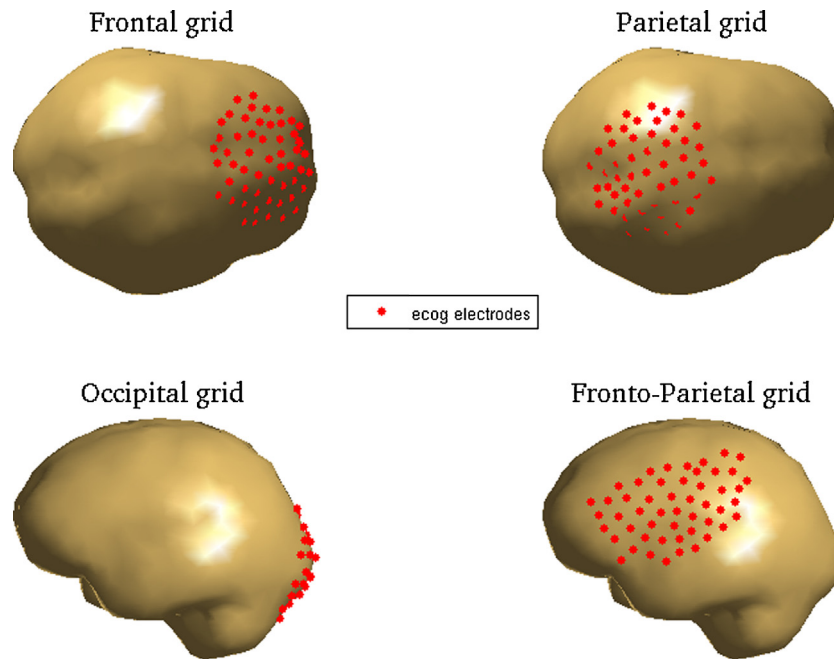
Fig. 1. The four synthetic grid configurations considered for the analysis of the numerical stability of the ECoG inverse problem.
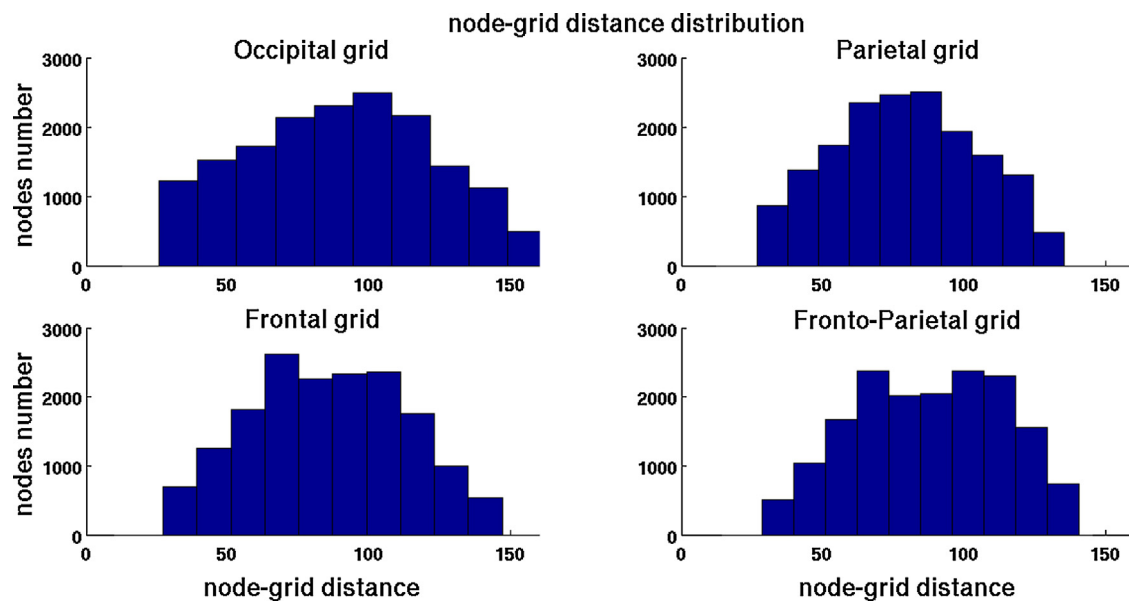

Fig. 2. Histograms of the number of source nodes for all values of the mean distance (in mm) between nodes and grid electrodes. For the occipital and fronto-parietal grids, many source nodes are far from the electrodes.

Table 1

Condition numbers of the lead-field matrices corresponding to four simulated ECoG grids and to a simulated EEG helmet with 60 electrodes. The source space is the same for the five simulations.

Position	Frontal	Parietal	Occipital	Fronto-Parietal	EEG
Condition number	20.9	8.0	92.5	31.2	598.29

centered at $t = 75$ ms and with standard deviation $\sigma = 20$ ms. Using our implementation for the ECoG forward model realized within the OpenMEEG software package, we computed the ECoG potentials for all four grids considered. We further added Gaussian white noise with mean value zero and varying standard deviations in such

a way that the signal-to-noise ratio of the data was 6, 4 and 1 dB, respectively (6 dB is a typical SNR value for an averaged ECoG time series, while 1 dB is close to the SNR of raw data). This procedure was repeated for all N dipoles ($N = 16{,}619$) placed at all nodes of the source space and oriented normally to the cortical surface. We then applied the LCMV beamformer to this set of synthetic waveforms, in order to reconstruct both the dipole location and its waveform. We found that for most dipoles, the localization error (defined as the Euclidean distance between ground-truth and reconstructed dipole positions) was zero (see Table 2 for the fraction of dipoles with non-zero error). This is expected because the simulation process was based on an "inverse crime", whereby the matrix used to generate the datasets was the lead-field matrix itself. Table 2 focuses on dipoles for which the localization error

Table 2
Reconstruction of a single source from synthetic data. For each grid and 3 distinct signal-to-noise ratios (SNRs): fraction of reconstructed dipoles with non-zero error localization, mean dipole-grid distance, mean localization error, and mean correlation coefficient between the reconstructed and the synthetic waveforms. The dipoles utilized in the experiment have strength of 0.02 nAm and time jitter of 20 ms.

Occipital	% Dipoles	Mean grid distance [mm]	Mean loc error [mm]	Mean corr. coeff.	SNR wave
SNR 6	0.19%	120.96 ± 23.73	6.68 ± 5.65	0.9995 ± 3.8e−05	40.6 ± 4.6
SNR 4	0.82%	121.66 ± 18.03	9.15 ± 9.44	0.9989 ± 1.2e−04	26.75 ± 3.33
SNR 1	25.1%	114.63 ± 22.08	17.84 ± 12.22	0.9833 ± 1.97e−03	6.28 ± 0.83
Parietal					
SNR 6	0.1%	111.29 ± 15.55	6.06 ± 4.77	0.9995 ± 5.4e−05	39.56 ± 3.66
SNR 4	0.37%	107.65 ± 15.06	7.02 ± 5.45	0.9989 ± 1.4e−04	25.9 ± 3.51
SNR 1	16%	101.86 ± 16.94	13.21 ± 9.40	0.9827 ± 1.91e−03	6.16 ± 0.82
Frontal					
SNR 6	0.1%	115.23 ± 11.37	6.83 ± 5.54	0.9995 ± 3.9e−05	40.21 ± 5.5
SNR 4	0.41%	112.95 ± 18.54	7.51 ± 5.11	0.9989 ± 1.1e−04	27.22 ± 3.40
SNR 1	20.1%	107.54 ± 18.57	14.67 ± 10.55	0.9838 ± 1.91e−03	6.4 ± 0.85
Fronto-Parietal					
SNR 6	0.22%	110.81 ± 17.02	8.33 ± 8.18	0.9995 ± 5.3e−05	40.52 ± 4.27
SNR 4	0.74%	112.47 ± 14.04	8.72 ± 5.71	0.9989 ± 1.3e−04	25.92 ± 3.45
SNR 1	22.34%	107.37 ± 17.15	16.54 ± 10.72	0.9826 ± 2e−03	6.15 ± 0.83
Whole-brain ECoG					
SNR 6	0				
SNR 4	0.02%		3.2 ± 0.65	0.9992 ± 6.423e−05	29.08 ± 4.8
SNR 1	1%		4.81 ± 3.1	0.985 ± 1.59e−03	6.7 ± 0.88
EEG					
SNR 6	0				
SNR 4	0				
SNR 1	0.53%		4.99 ± 2.43	0.985 ± 1.49e−03	6.62 ± 0.81

was non-zero and includes the following entries: (1) the fraction of dipoles with non-zero error (% dipoles); (2) the dipole-grid distance (mean grid distance) defined as the mean distance between a dipole and all grid electrodes; (3) the mean and standard deviation of the localization error (mean loc error); (4) the mean and standard deviation of the correlation coefficients between the simulated and reconstructed waveforms (mean corr coeff). Table 2 also includes results for the analysis of two more simulated dataset. In the first case the new routine in OpenMEEG is used to compute the electric potential on the 60 sensors of a simulated ECoG grid that cover the whole brain. This analysis was performed in order to better understand how the partial spatial coverage of a realistic ECoG grid affects localization accuracy. In the second case we used OpenMEEG to compute the synthetic electric potential virtually recorded on the scalp by a simulated 60-channel EEG that cover the whole head. This analysis was performed in order to assess to what extent the localization inaccuracies are induced by skull-related signal attenuation. Finally, Fig. 3 shows the mean source distance from the ECoG grid versus the mean localization error for the four synthetic partial-coverage grids and the three values of the SNR. In order to verify whether there is some preferential direction according to which the beamformer reconstructs the source, in Fig. 4 we have compared the distance of the reconstructed dipole from the grid with the distance of the ground-truth source from the grid.

In the second experiment, we generated 3000 dipole pairs using the following simulation paradigm:

- The positions of the two dipoles were randomly sampled in the source space (i.e., on the nodes of the cortical grid) for each pair in an independent fashion.
- The minimum distance between the two dipoles for each pair was set to 2 cm.
- The dipole waveforms had strength of 0.02 nAm and time jitter of 20 ms and were further designed to satisfy three different correlation levels (1000 pairs each level): $r = 0$, 0.6 and 1 (we used the same Gaussian waveform for the two dipoles and considered three different time delays between the two waveforms, i.e. 0 ms, 50 ms, and 150 ms, respectively).

Again, we used OpenMEEG for generating the electrodes potentials on the usual four ECoG grids and added Gaussian noise to reach in all 3000 cases a signal-to-noise ratio of around 5 dB.

For each experiment we studied when: (1) both dipoles in the pair were correctly localized (i.e., the localization error was zero); (2) only one dipole was correctly localized (i.e., the localization error for the other dipole was non-zero); (3) both dipoles were incorrectly localized (i.e., the localization error for both dipoles was non-zero). Table 3 reports the mean localization errors for the three correlation levels. Fig. 5 describes the impact of these correlations on the reconstruction accuracy measured as the fraction of dipoles that are correctly localized. We have also considered a further experiment where pre-stimulus noise was added to the synthetic signal as if recorded by the grid utilized in the real experiment described below but, this time, the dipoles' waveform had an amplitude of 10 nAm and a time jitter of 10 ms. The results of such experiment are again in Table 3 and in Fig. 6.

3.3. Analysis of experimental data

We finally analyzed an experimental dataset recorded from one subject during a rapid visual categorization task. The subject was a patient with pharmacologically intractable epilepsy treated at Children's Hospital Boston (CHB) and implanted with intracranial electrodes to localize seizure foci for potential surgical resection. The study was approved by the hospital's institutional review board and was carried out with the subjects' informed consent. Electrode locations were driven by clinical considerations.

The experimental paradigm is shown in Fig. 7 (left panel) Each one of the 320 trials started with the presentation of a stimulus, i.e., a grayscale image (256 × 256 pixels) subtending about 7° × 7° of visual angle. The stimulus set used was a subset of the image dataset used in (Serre et al., 2007). The stimulus was presented for 34 ms and was followed by a blank screen for another 34 ms (SOA: 68 ms). After this, the response period started, characterized by the presentation of a fixation cross on a uniform mid-gray image. Data were collected using a grid made of three strips placed on the parietal-occipital lobe of the right hemisphere and composed of 64 electrodes (Fig. 7, right panel). The data was epoched for a duration
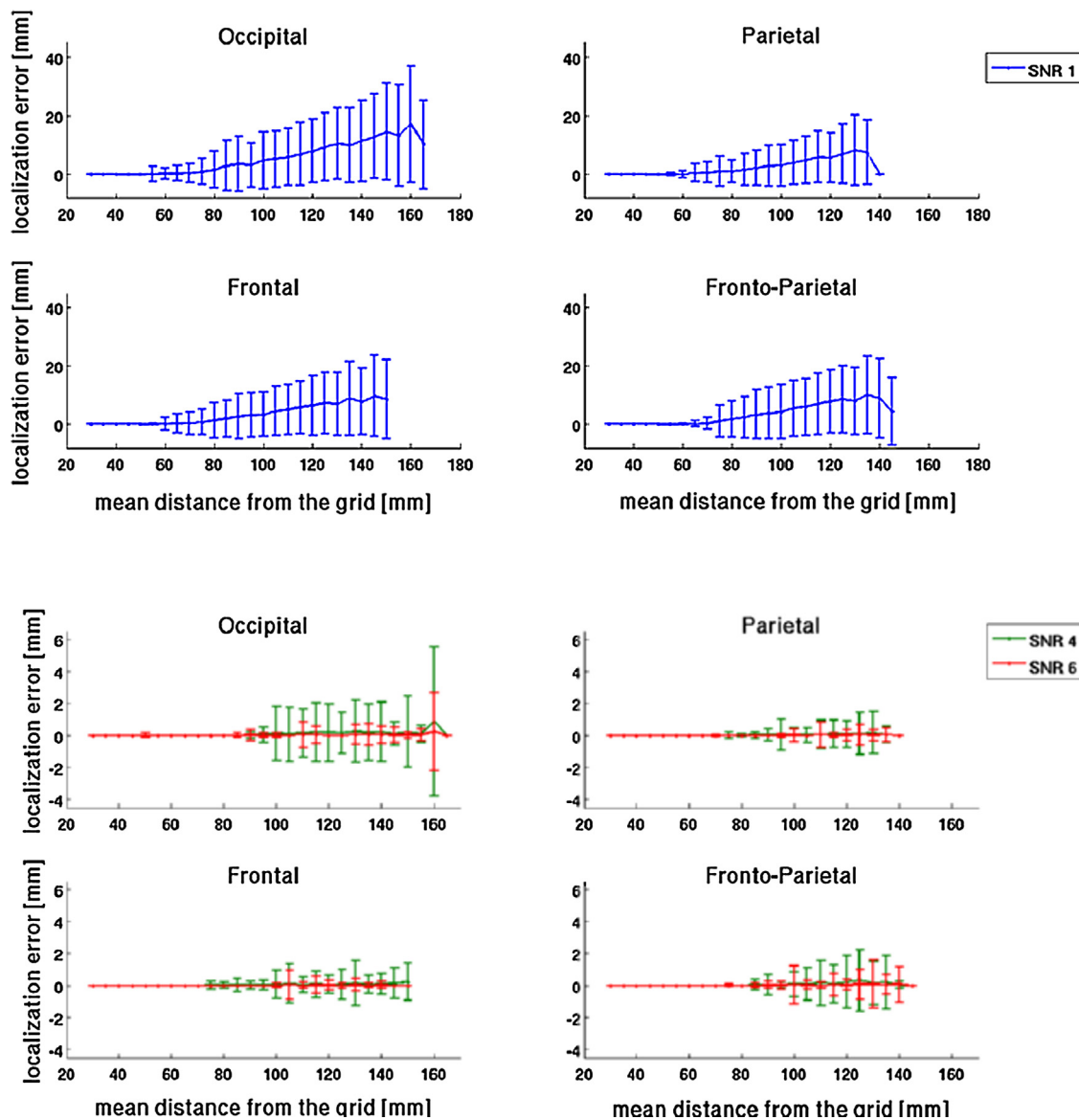
Fig. 3. Behavior of the localization error versus the mean source distance from the sensors for the four synthetic grids and the three SNR levels. The localization error has been averaged over the number of dipoles reconstructed at each binned distance from the grid. The bars correspond to the standard deviations.

of 850 ms around the stimulus onset (baseline: 200 ms; sampling frequency 250 Hz; 217 time-points). The grand average for each electrode over epoch led to a data matrix V with size 64×217. We then co-registered the sensors' positions on the individual brain segmented by Freesurfer (Dale et al., 1999) and characterized by $N = 20{,}484$ cortical nodes. The size of the resulting lead-field matrix L was therefore $64 \times 20{,}484$. A straightforward SVD analysis showed that the condition number for this matrix was around 100.83.

The LCMV beamformer was used to reconstruct the source location for these data as the local maximum of the neural activity index in Eq. (10) and the corresponding waveforms given in Eq. (5).

Fig. 8 shows the result of the analysis at 120 ms latency. Specifically, the panels in the first column highlight two activation peaks in the neural index map. The panels in the second peak compare the corresponding reconstructed waveforms with the signals recorded by the two ECoG channels closest to the maxima in the neural index map. Fig. 9 contains 15 intensity maps reconstructed every 20 ms starting at 94 ms latency. The Talairach coordinates corresponding to the positions of the activation peaks in the neural index

map together with the corresponding brain area are illustrated in Table 4.

4. Discussion and conclusions

The first result achieved in this paper has been the implementation of a new function that allows the user to account for a three-compartment head (scalp, skull, and brain) in ECoG experiments. This is a helpful tool since, differently from MEG and similarly to EEG, ECoG is rather sensitive to volume currents and therefore accounting for the presence of the three layers in the computation of the lead-field matrix leads to a more reliable model.

Then we have conducted a quantitative analysis of the numerical stability of the ECoG source-modeling problem, which is independent of the type of inversion algorithm used for localization. Assessing numerical stability requires the computation of the condition number of the lead-field matrix. We used this approach for a forward model computed by means of a symmetric BEM that was implemented within the OpenMEEG framework and found that:
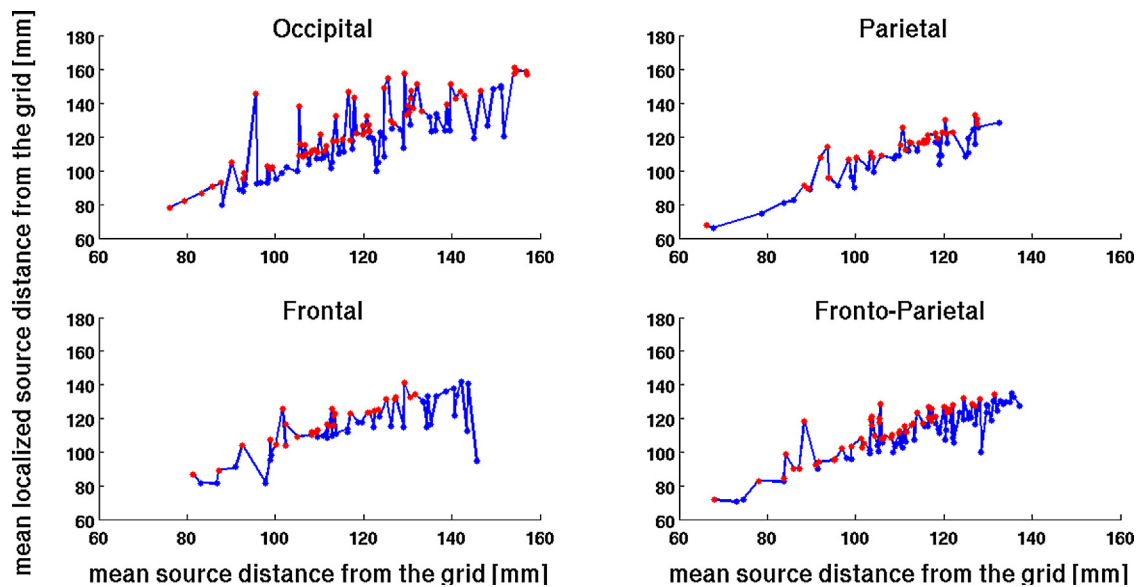
Fig. 4. Behavior of the mean reconstructed source distance from the grid versus the mean source distance from the sensors for the four synthetic grids and SNR level of 5 dB. The red dots indicate the case where the reconstructed source is far from the grid with respect the real one, while the blue dots correspond to the opposite case. (For interpretation of the references to color in this figure legend, the reader is referred to the web version of this article.)

Table 3

Reconstruction of dipole pairs: mean localization error for each dipole in the pair for three levels of correlation. The 'Occipital', 'Parietal', 'Frontal', and 'Fronto-Parietal' cases are concerned with dipoles with strength of 0.02 nAm and time jitter of 20 ms. The 'Real ECoG grid' case is concerned with the same grid as in the real experiment described below and the dipoles have strength of 10 nAm and time jitter of 10 ms.

Occipital						
	2 reconstructed dipoles [mm]		1 reconstructed dipole [mm]		0 reconstructed dipoles [mm]	
NO corr	0	0	0	70.61 ± 31.95	21.91 ± 17.25	25.52 ± 22.13
Partial corr	0	0	0	70.10 ± 32.59	31.64 ± 19.54	26.33 ± 19.66
corr	0	0	0	80.88 ± 28.91	45.87 ± 32.79	42.25 ± 31.96
Parietal						
NO corr	0	0	0	67.27 ± 33.70	18.06 ± 10.76	22.012 ± 15.86
Partial corr	0	0	0	66.85 ± 37.35	18.81 ± 11.25	22.68 ± 19.78
corr	0	0	0	78.28 ± 30.03	46.16 ± 34.08	46.89 ± 33.75
Frontal						
NO corr	0	0	0	69.04 ± 34.63	19.58 ± 14.17	26.08 ± 19.86
Partial corr	0	0	0	65.57 ± 35.35	19.67 ± 18.20	29.22 ± 18.37
corr	0	0	0	84.97 ± 27.95	46.31 ± 33.22	44.06 ± 33.8
Fronto-Parietal						
NO corr	0	0	0	68.69 ± 33.75	32.63 ± 24.73	23.90 ± 19.25
Partial corr	0	0	0	66.21 ± 35.01	25.67 ± 25.11	27.41 ± 20.01
corr	0	0	0	80.83 ± 28.36	44.96 ± 34.27	44.93 ± 33.96
Real ECoG grid						
NO corr	0	0	0	74.82 ± 29	31.76 ± 25.31	33.51 ± 26.14
Partial corr	0	0	0	76.1 ± 28.74	31.94 ± 29.39	37.78 ± 26.32
corr			0	82.64 ± 26.50	43.52 ± 31.92	40.09 ± 30.72

- For all four ECoG grids considered, the condition number was below 10^2, i.e. typical of mildly ill-conditioned problem (John, 1960), and one order of magnitude smaller than that the one associated with the forward model of a typical high-density EEG helmet (see Table 1).
- The condition number for the four grids increased coherently with the average distance between the source nodes and the grids (see the histograms in Fig. 2).

In particular, the occipital grid is associated with the worst condition number and collects information from the most distant sources (up to 20 cm); the parietal grid has the best conditioning and in this case the most distant source is just 14 cm from the electrodes.

We then performed the source modeling of both synthetic and experimental ECoG data by means of an LCMV beamforming algorithm. Beamformers are currently the most frequently used inversion methods in neurophysiology and the LCMV implementation has proven its effectiveness for a number of data analysis studies in both EEG and MEG. In the case of uncorrelated sources, beamformers have a rather similar (although more focused) behavior with respect to L2-regularization methods like the one at the basis of sLORETA, another frequently applied method; in the case of time correlated sources, sLORETA typically outperforms beamforming. In order to compare across different ECoG grids and between the ECoG and EEG modalities, we first considered two 'inverse crime' experiments: synthetic data were generated by means of the same forward model applied for the inversion. The first experiment focused on the reconstruction of a single source and studied how much information can be extracted from the limited amount of cortical data provided by ECoG grids in different positions (Table 2). Our results suggest that for high signal-to-noise ratios (close to the ones typical of averaged time series), source localization failed less than 0.1% times with an average localization
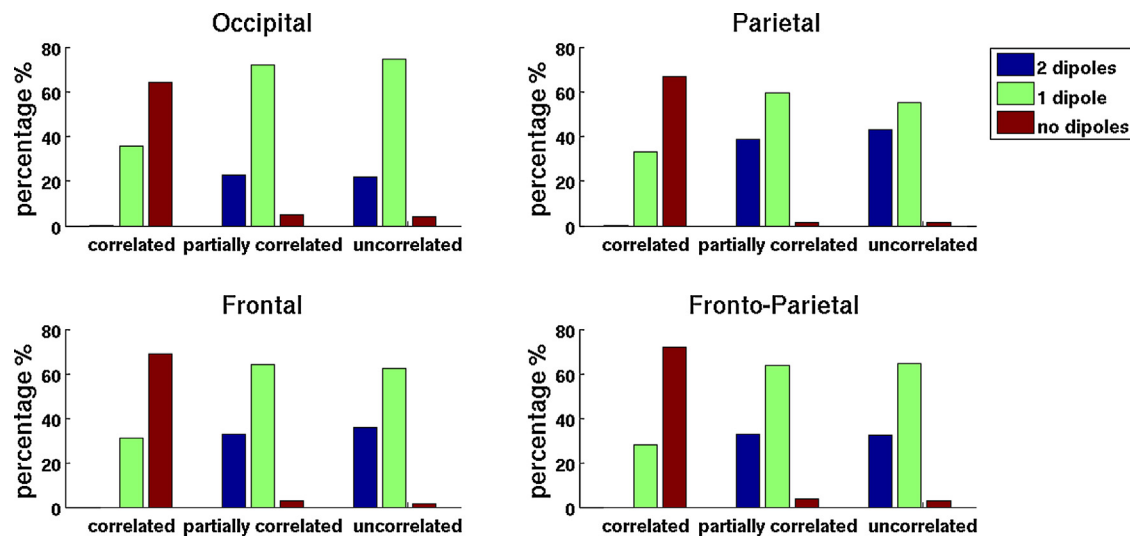
Fig. 5. Reconstruction of dipole pairs: rate of exactly localized dipoles with respect to the correlation degree of the two dipoles' waveforms. Correlated waveforms are two Gaussian forms with zero time delay; partially correlated waveforms have time delay equal to 50 ms; not-correlated waveforms have time delay equal to 150 ms.
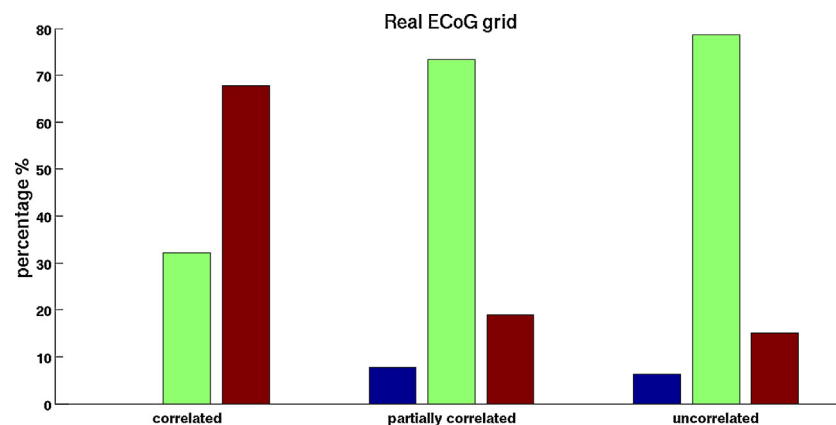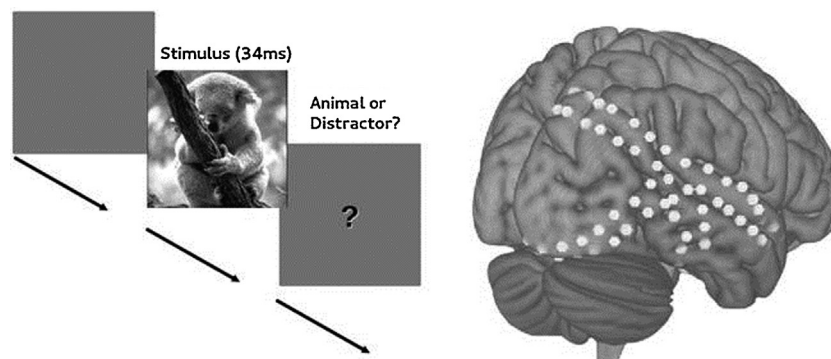

Fig. 6. Reconstruction of dipole pairs in the case of real ECoG grid: rate of exactly localized dipoles with respect to the correlation degree of the two dipoles' waveforms. Correlated waveforms are two Gaussian forms with zero time delay; partially correlated waveforms have time delay equal to 50 ms; not-correlated waveforms have time delay equal to 150 ms.

Fig. 7. Acquisition of experimental data evoked by a visual recognition task. Left panel: the visual stimulus and the experimental paradigm. Right panel: the ECoG grid co-registered on the individual brain.

error always below 1 cm. At lower signal-to-noise ratios (closer to the ones typical of raw data), the failure rate increased up to 25% (for the occipital grid) and, correspondingly, the mean localization error over the whole cortex approached 2 cm (we repeated this experiment also by using neural noise obtained by adding the pre-stimulus signal of the real dataset to the synthetic field; in this simple one-dipole case, this results in a very high SNR so that all dipoles are always correctly reconstructed). We also computed the rate of dipoles for which the localization error is bigger than 2 cm; at the lowest SNR these rate are: 9% for occipital grid, 3% for parietal grid, 5% for frontal grid and 6.78% for the fronto-parietal one with a mean grid distance of at least 10 cm. The correlation coefficient
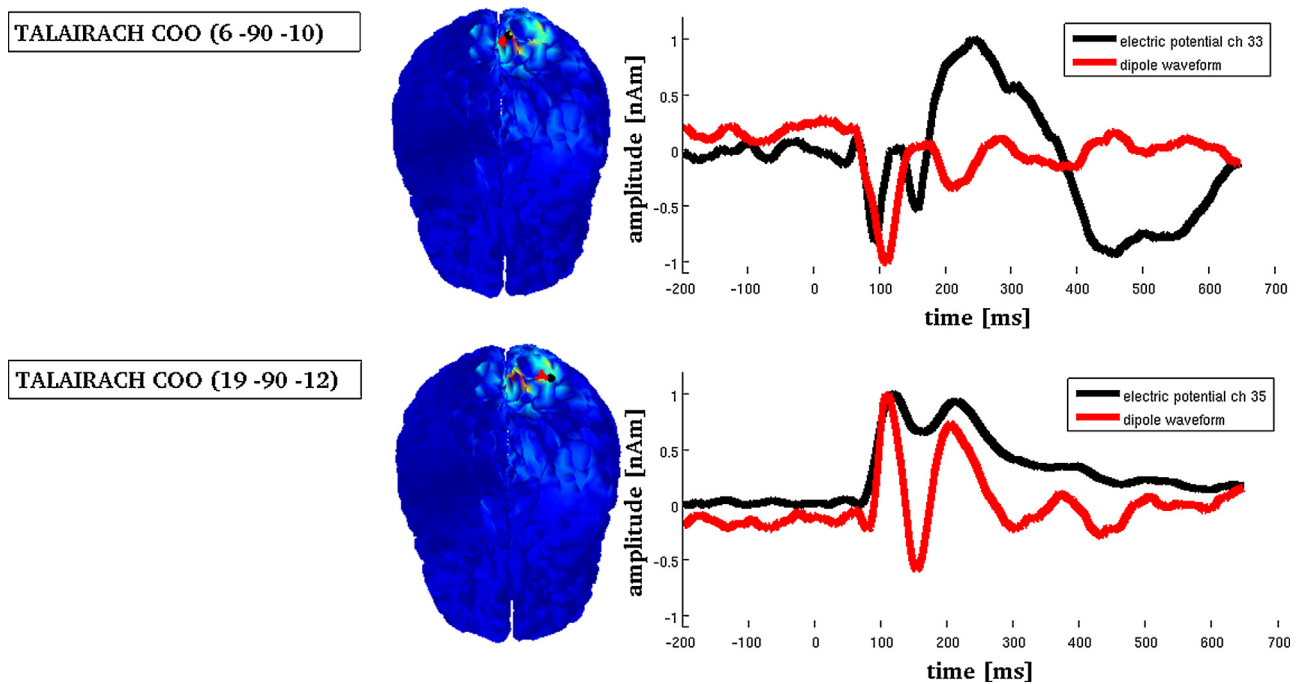
Fig. 8. Source modeling of the ECoG data evoked by the categorization task. Left panels: neural index at time 120 ms with two different peak intensities highlighted together with the respective Talairach coordinates. Right panels: reconstructed waveforms for the dipoles located in correspondence of the two red diamonds in the neural index map and the electric potentials recorded by the grid's channels closest to the reconstructed dipoles (the two waveforms have been normalized for comparison purposes).
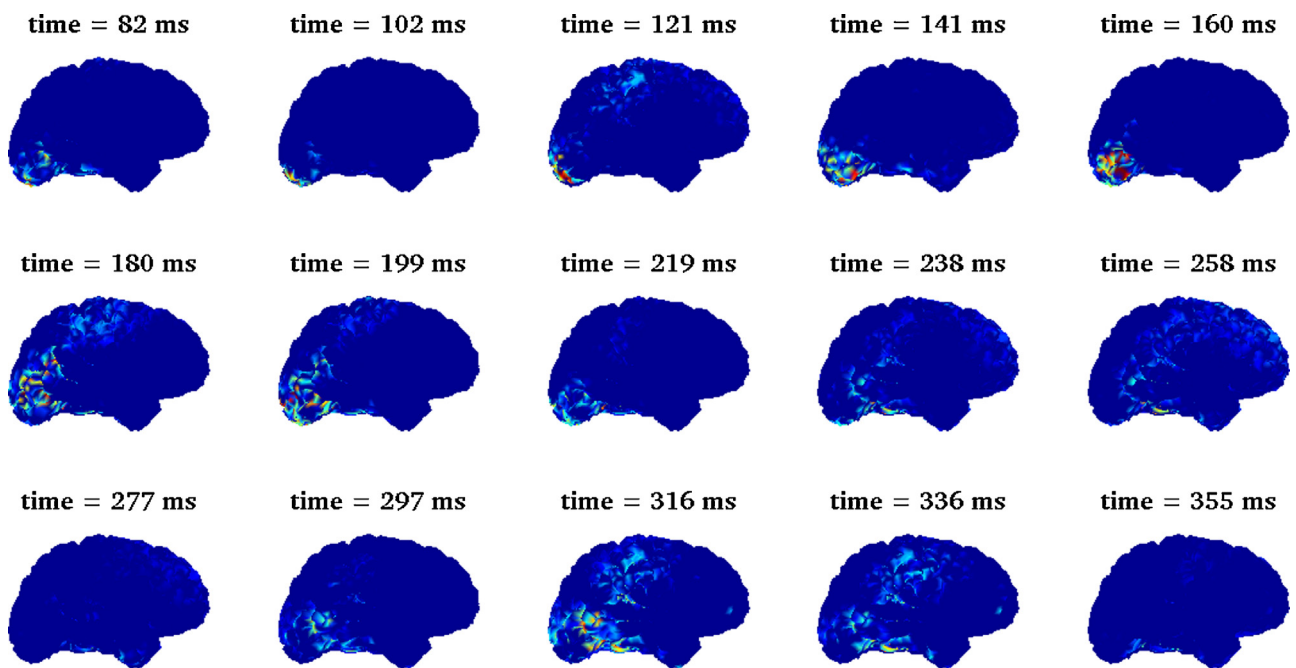

Fig. 9. Source modeling of the ECoG data during a categorization task: Intensity maps every 16 ms within a 100–240 ms time window.

between the simulated and reconstructed waveforms was almost always close to 1. This is probably due to the fact that, as in Sekihara et al. (2002), we have projected the beamformer weight onto the signal subspace. These results demonstrate an effective restoration of the dipole's waveform with little sensitivity to the grid position. In this experiment we also compared the results provided by the LCMV beamformer when the ECoG signal is recorded using partial-coverage ECoG grids with respect to the case of an (un-realistic) ECoG grid covering the whole brain and of a (realistic) 60-channel whole-head EEG helmet. This comparison allowed us to assess the

impact on the reconstruction accuracy induced by either a partial coverage of the brain as it happens in typical ECoG experiments or signal attenuation due to the skull when data are recorded on the scalp by an EEG device. The results show that the partial coverage of the cortex may deteriorate the reconstruction effectiveness and accuracy of more than 100%, independently of signal attenuation induced by the skull and at all SNR levels. Moreover, Fig. 3 provides a quick assessment of the localization accuracy as a function of the distance from the grid's sensors. This analysis shows that 60–80 mm is a critical distance for the localization power of

Table 4
Talairach coordinates and corresponding brain areas for the activation maps in Fig. 9.

T	Coo Talairach	Source amplitudes (nAm)	Region
82	(−9 −97 −11)	−100.54	Left, Occipital Lobe, Lingual Gyrus, BA 17
102	(6 −90 −10)	−189.73	Right, Occipital Lobe, Lingual Gyrus, BA 17/18
121	(17 −94 −8)	152.92	Right, Occipital Lobe, Lingual Gyrus, BA 18
141	(27 −89 −7)	−120.93	Right, Occipital Lobe, Inferior Occipital Gyrus, BA 18
160	(38 −76 −3)	115.18	Right, Occipital Lobe, Inferior Occipital Gyrus, BA 19
180	(38 −83 5)	88.614	Right, Occipital Lobe, Middle Occipital Gyrus, BA 19
199	(27 −82 −5)	127.34	Right, Occipital Lobe, Middle Occipital Gyrus, BA 18
219	(27 −82 −5)	122.11	Right, Occipital Lobe, Middle Occipital Gyrus, BA 18
238	(27 −82 −5)	92.842	Right, Occipital Lobe, Middle Occipital Gyrus, BA 18
258	(32 −50 3)	66.609	Right, Limbic Lobe, Parahippocampal Gyrus, BA 19
277	(41, −20, −23)	−22.467	Right, Temporal Lobe, Fusiform Gyrus, BA 20
297	(41, −74, 4)	45.878	Right, Occipital Lobe, Middle Occipital Gyrus, BA 19
316	(41, −74, 4)	55.382	Right, Occipital Lobe, Middle Occipital Gyrus, BA 19
336	(31, −34, −9)	−42.449	Right, Limbic Lobe, Parahippocampal Gyrus, BA 36
355	(36, −27, −18)	−31.542	Right, Limbic Lobe, Parahippocampal Gyrus, BA 36

beamforming to begin to deteriorate. Finally, the results in Fig. 4 shows that the reconstructions provided by the beamformer occur with no direction bias.

The second experiment performed a validation of the beamformer in the case of synthetic data associated to dipole pairs with random positions on the cortex (Table 3). We found that, if both dipoles in the pair were within 70 mm average distance from the grid, the localization error was null; if one of the two dipoles was within a 70 mm average distance from the grid and the other one was within 110 mm average distance, we localized exactly only the source nearest to the grid; if both dipoles were within 110 mm average distance from the grid, we could not localize exactly any of the sources. In the case when only one dipole was correctly localized, the localization error for the other dipole tended to be rather large (larger than the localization error when both dipoles in the pair were not precisely localized). This may be explained by the fact that the precisely localized source, which was closest to the sensor grid, produced a stronger ECoG field that masked the field produced by the other source. We found this trend to hold for all grids (also in the case of the synthetic data recorded by the real grid), and whether the sources were not or partially correlated in time. When the sources were perfectly correlated in time the beamformer method failed to reconstruct any of the dipoles in the pair; indeed as shown in Figs. 5 and 6 the number of dipole pairs correctly localized was almost zero while the number of cases for which neither source was correctly localized was very high. This behavior is consistent with previous results suggesting that beamformers are sensitive to correlated data (Pascarella et al., 2010).

The experimental data processed in this paper were potentials evoked during a visual categorization task. The results of the inversion analysis showed that it is possible to use ECoG to detect a very early activation in the occipital region of the left hemisphere while all other activations are reconstructed in the right hemisphere. However the reconstruction at 120 ms in V1, which should be bi-lateral, misses the one component on the left hemisphere, and this is most likely due to the well-established susceptibility of beamforming to temporal correlation (Quraan and Cheyne, 2010). Specifically, the reconstructed brain activations (Table 4) reflect the flow of information from occipital areas toward more anterior areas along the temporal lobe, which seems consistent with both invasive monkey electrophysiology studies (DiCarlo et al., 2012; Mormann et al., 2008; Liu et al., 2009) and non-invasive (MEG and fMRI) human studies (Cichy et al., 2014). However, not all the reconstructed information in this flow is reliable. In fact, we have generated the synthetic fields associated to all sources in the stream and projected them back with the beamformer. We found that all sources with latencies from 102 ms to 238 ms are correctly reproduced, while the ones with higher latency are missing by the beamformer-ECoG modality.

Overall, the results of both simulations and the real experiment show that the use of beamformers for modeling sources from ECoG data should be considered with great caution. When the source configuration becomes more complex than in the one-dipole toy case the reconstruction accuracy rapidly deteriorates, particularly when the grid is placed in the occipital region. Further, coherently with what results from also EEG and MEG literature, such deterioration becomes really notable when the time correlation between sources increases. These results suggest that other inversion techniques, for example like the ones formulated in Bayesian frameworks (Sorrentino et al., 2009; Sommariva and Sorrentino, 2014), should be considered for this kind of analysis.

Acknowledgments

References

Brookes MJ, Stevenson CM, Barnes GR, Hillebrand A, Simpson MI, Francis ST, et al. Beamformer reconstruction of correlated sources using a modified source model. Neuroimage 2007;34(4):1454–65.

Cho JH, Hong SB, Jung YJ, Kang HC, Kim HD, Suh M, et al. Evaluation of algorithms for intracranial EEG (iEEG) source imaging of extended sources: feasibility of using iEEG source imaging for localizing epileptogenic zones in secondary generalized epilepsy. Brain Topogr 2011;24(2):91–104.

Cichy RM, Pantazis D, Oliva A. Resolving human object recognition in space and time. Nat. Neurosci 2014;17(3):455–62.

Dale AM, Fischl B, Sereno MI. Cortical surface-based analysis: I. Segmentation and surface reconstruction. Neuroimage 1999;9(2):179–94.

DiCarlo JJ, Zoccolan D, Rust NC. How does the brain solve visual object recognition? Neuron 2012;73(3):415–34.

Fuchs M, Wagner M, Kastner J. Development of volume conductor and source models to localize epileptic foci. J Clin Neurophysiol 2007;24(2):101–19.

Dümpelmann M, Fell J, Wellmer J, Urbach H, Elger CE. 3D source localization derived from subdural strip and grid electrodes: a simulation study. Clin Neurophysiol 2009;120(6):1061–9.

Dümpelmann M, Ball T, Schulze-Bonhage A. sLORETA allows reliable distributed source reconstruction based on subdural strip and grid recordings. Hum Brain Mapp 2012;33(5):1172–88.

Golub GH, Van Loan CF. Matrix computations. Baltimore, MD, USA: Johns Hopkins University Press; 1996. p. 374–426.

Gramfort A, Papadopoulo T, Olivi E, Clerc M. OpenMEEG: opensource software for quasistatic bioelectromagnetics. Biomed Eng Online 2010;9(1):45.

Hämäläinen M, Hari R, Ilmoniemi RJ, Knuutila J, Lounasmaa OV. Magnetoencephalography—theory, instrumentation, and applications to noninvasive studies of the working human brain. Rev Mod Phys 1993;65(2):413.

Hämäläinen MS, Ilmoniemi RJ. Interpreting measured magnetic fields of the brain: estimates of current distributions. Helsinki University of Technology: Department of Technical Physics; 1984.

Hillebrand A, Barnes GR. Beamformer analysis of MEG data. Int Rev Neurobiol 2005;68:149–71.

Huiskamp GJM. Inverse and forward modeling of interictal spikes in the EEG, MEG and ECoG. In: Engineering in medicine and biology, 2002 IEEE 24th annual conference and the annual fall meeting of the biomedical engineering society EMBS/BMES conference, 2002. Proceedings of the second joint (Vol. 2); 2002. p. 1393–4.

John F. Continuous dependence on data for solutions of partial differential equations with a prescribed bound. Commun Pure Appl Math 1960;13:551–85.

Kybic J, Clerc M, Abboud T, Faugeras O, Keriven R, Papadopoulo T. A common formalism for the integral formulations of the forward EEG problem. IEEE Trans Med Imaging 2005;24(1):12–28.

Liu H, Agam Y, Madsen JR, Kreiman G. Timing, timing, timing: fast decoding of object information from intracranial field potentials in human visual cortex. Neuron 2009;62(2):281–90.

Michel CM, Murray MM, Lantz G, Gonzalez S, Spinelli L, Grave de Peralta R. EEG source imaging. Clin Neurophysiol 2004;115(10):2195–222.

Mormann F, Kornblith S, Quiroga RQ, Kraskov A, Cerf M, Fried I, et al. Latency and selectivity of single neurons indicate hierarchical processing in the human medial temporal lobe. J Neurosci 2008;28(36):8865–72.

Mosher JC, Lewis PS, Leahy RM. Multiple dipole modeling and localization from spatio-temporal MEG data. IEEE Trans Biomed Eng 1992;39(6):541–57.

Mosher JC, Leahy RM. Recursive MUSIC: a framework for EEG and MEG source localization. IEEE Trans Biomed Eng 1998;45(11):1342–54.

Mosher JC, Leahy RM. Source localization using recursively applied and projected (RAP) MUSIC. IEEE Trans Signal Process 1999;47(2):332–40.

Pascarella A, Sorrentino A, Campi C, Piana M. Particle filtering, beaforming and multiple signal classification for the analysis of magnetoencephalography time series: a comparison of algorithms. Inverse Probl Imaging 2010;4:169–90.

Quraan MA, Cheyne D. Reconstruction of correlated brain activity with adaptive spatial filters in MEG. Neuroimage 2010;49(3):2387–400.

Quraan MA. Characterization of brain dynamics using beamformer techniques: advantages and limitations. INTECH Open Access Publisher; 2011.

Schalk G, Leuthardt EC. Brain-computer interfaces using electrocorticographic signals. IEEE Rev Biomed Eng 2011;4:140–54.

Schuh L, Drury I. Intraoperative electrocorticography and direct cortical electrical stimulation. In: Seminars in anesthesia, perioperative medicine and pain (Vol. 16, No. 1, pp. 46–55). WB Saunders; 1997.

Sekihara K, Nagarajan SS, Poeppel D, Marantz A, Miyashita Y. Reconstructing spatio-temporal activities of neural sources using an MEG vector beamformer technique. IEEE Trans Biomed Eng 2001;48(7):760–71.

Sekihara K, Nagarajan SS, Poeppel D, Marantz A, Miyashita Y. Application of an MEG eigenspace beamformer to reconstructing spatio-temporal activities of neural sources. Hum Brain Mapp 2002;15(4):199–215.

Serre T, Oliva A, Poggio T. A feedforward architecture accounts for rapid categorization. Proc. Natl. Acad. Sci 2007;104(15):6424–9.

Sommariva S, Sorrentino A. Sequential Monte Carlo samplers for semi-linear inverse problems and application to Magnetoencephalography. Inverse Probl 2014;30:114020.

Sorrentino A, Parkkonen L, Pascarella A, Campi C, Piana M. Dynamical MEG source modeling with multi-target Bayesian tracking. Hum Brain Mapp 2009;30:1911–21.

Spencer ME, Leahy RM, Mosher JC, Lewis PS. Adaptive filters for monitoring localized brain activity from surface potential time series. In: IEEE 1992 conference record of the twenty-sixth asilomar conference on signals, systems and computers; 1992. p. 156–61.

Thorpe S, Fize D, Marlot C. Speed of processing in the human visual system. Nature 1996;381(6582):520–2, http://dx.doi.org/10.1038/381520a0.

Van Veen BD, van Drongelen W, Yuchtman M, Suzuki A. Localization of brain electrical activity via linearly constrained minimum variance spatial filtering. IEEE Trans Biomed Eng 1997;44(9):867–80.

Zhang Y, van Drongelen W, Kohrman M, He B. Three-dimensional brain current source reconstruction from intra-cranial ECoG recordings. Neuroimage 2008;42(2):683–95.